

## Modeling the Fractal Growth of Templated, Mesoporous Silica Films

Karen J. Edler,<sup>†</sup> Matthew Arrowsmith,<sup>‡</sup> Martin Hamilton,<sup>‡</sup> and Sean P. Rigby<sup>\*,‡</sup>

Department of Chemistry and Department of Chemical Engineering, University of Bath,  
Claverton Down, Bath, BA2 7AY, United Kingdom

Received: October 14, 2004; In Final Form: January 11, 2005

Brewster angle micrographs have been obtained of the development of a silica film grown at an air–water interface with use of the surfactant template cetylpyridinium chloride. The micrograph images showed that the growing silica film exhibited complex, fractal-like patterns. These images have been analyzed to determine the values of the fractal dimension and lacunarity, and the forms of the autocorrelation function and Euclidean crossover behavior of the silica clusters have been observed. These statistical descriptors have been compared with the equivalent properties of simulated images of model structures generated by computer using a particular variant of the cluster–cluster aggregation (CCA) algorithm. Good agreement was found between the characteristic properties of typical experimental images and the simulated images. It was, therefore, suggested that the CCA process is a good model for the growth of the silica films.

### Introduction

Thin, porous, silica films, with controlled pore sizes obtained by templating techniques, have many potential applications, such as membranes for advanced reactors and separators. To obtain the desired properties for the film it is necessary to tightly control the manufacturing process. To be able to do this it is essential to fully understand the physical processes involved in film synthesis and manufacture. The structure of the film at every length scale is important in determining its potential utility. Both pore-scale and larger scale film structure will influence its mass transport properties and mechanical stability.

Mesostructured silica-surfactant films were first grown from solution by using cetyltrimethylammonium bromide (CTAB) or chloride surfactants,<sup>1</sup> and much work has been done to determine the structure and growth mechanisms of those films.<sup>2</sup> However, CTAB films are all very rough and opaque and uniformly cover the surface of the solution, with none of the complex, and potentially interesting, fractal structures that have been observed (see below) for films synthesized with use of cetylpyridinium chloride (CpCl). Little previous work has investigated the use of different surfactants in the silica-surfactant systems that form films at the air–water interface. The synthesis of smooth, optically clear, films would be more interesting for applications in encapsulation, and films possessing fractal morphologies might be useful for production of membranes with multimodal porosity over various length scales (e.g. macro- and microporosity). As will be seen below, CpCl produces both these types of film structure depending on concentration. The technique of growing mesostructured films at the air–solution interface has recently been extended to TiO<sub>2</sub> and ZrO<sub>2</sub> films,<sup>3</sup> using anionic surfactants, but no studies have been made of their macroscopic structures (only the mesostructures).

As mentioned above, the macroscopic structure of the silica films grown in this work appears to possess fractal character-

istics. The growth of thin films that have fractal morphology has been studied on a variety of different surfaces. Schwartz et al.<sup>4</sup> studied the self-assembly of monolayers of octadecyltrichlorosilane on mica surfaces using AFM. Fractal dimensions were obtained from the images by using the box-counting algorithm. It was found that with increasing coverage the fractal dimension of the growing domains evolved from 1.6 to 1.8. The structures of the aggregates were simulated by using a multigrowth center diffusion-limited aggregation (DLA) model. The evolution in fractal dimension was attributed to changes in the growth kinetics. Fractal clusters that resembled patterns formed by cluster–cluster aggregation were studied by Carrière et al.<sup>5</sup> in gold films deposited on amorphous Al<sub>2</sub>O<sub>3</sub> supported on carbon-coated mica surfaces. Fractal dimensions of these clusters were measured via the density–density correlation functions of digitized TEM images. In many cases<sup>6</sup> a particular mechanism for the formation of a fractal cluster is attributed to a real system based solely on a comparison of the fractal dimension of a model structure with that of a real structure. However, most real aggregates are too complex to be completely described by solely a single fractal dimension. These structures often exhibit multifractality or crossover effects. In this work the fractal dimension descriptor will be supplemented by the lacunarity parameter (described below) and a study of the forms of the mass autocorrelation function and Euclidean crossover behavior for clusters, to more confidently assign a particular definitive mechanism for fractal growth.

### Experimental Section

Films were grown at room temperature at the solution/air interface in small Teflon troughs, 3 mm deep, having a surface area of 63 cm<sup>2</sup>. The film forming solution was prepared by dissolving cetylpyridinium chloride (CpCl, Sigma 98%) in 0.2 M HCl solution prepared by using deionized water purified to 18 M $\Omega$  cm. Once the surfactant was dissolved, tetramethoxysilane (TMOS, Aldrich 98%) was added and the solution sealed and shaken until homogeneous (less than 1 min). The molar ratio used to obtain a “fractal film” was  $8.143 \times 10^{-4}$  CpCl:  $1.18 \times 10^{-2}$  TMOS:  $3.63 \times 10^{-3}$  HCl: 1 H<sub>2</sub>O. This solution was

\* Corresponding author. E-mail: s.p.rigby@bath.ac.uk. Phone: +44 (0)-1225 384978. Fax: +44 (0)1225 385713.

<sup>†</sup> Department of Chemistry.

<sup>‡</sup> Department of Chemical Engineering.

poured into the Teflon trough mounted on a Brewster angle microscope (NFT-BAM2, Nanofilm Technologie GmbH) such that images could be taken as the film grew at the air–solution interface. Images were taken of the growing film at intervals ranging from 20 min during the induction period to 30 s during the period of rapid film growth. The images were corrected by subtracting a reference image to account for the nonuniform illumination by the laser beam across the image. Silica-surfactant film growth from these solutions is reported in more detail by Edler et al.<sup>7</sup> The image contrast consisted of 256 gray levels.

## Theory

**Fractal Models of Aggregates.** Fractals are objects that possess the special property of self-similarity, where increasing magnifications reveal similar structures over many length scales. There are several objects, such as the Sierpinski gasket or the Menger sponge, which possess the symmetry of self-similarity exactly, where they are invariant under uniform changes of length scale in all “directions”. These objects can be exactly mapped onto themselves after a change of length scales. Unfortunately, these objects do not represent, at all well, most objects occurring in Nature. However, there are other classes of objects which, while not being invariant to most symmetry operators (rotation, reflection, etc.) associated with Euclidean geometry and cannot be mapped onto themselves after a change of length scales, do retain an important vestige of both the symmetry of self-similarity and some of the symmetries of Euclidean geometry. These objects are said to be *statistically* self-similar fractals, because all of the statistical quantities that can be used to characterize them are invariant to a change of length scales. Statistically self-similar fractals can be used to model various aggregation processes.

A wide range of cluster growth algorithms have been developed. These models include diffusion-limited aggregation (forming DLAs) and cluster–cluster aggregation (forming CCAs). The original diffusion-limited aggregation model, developed by Witten and Sandler,<sup>8</sup> was stimulated by earlier experimental work on the aggregation of small metal particles in a dense gas.<sup>9</sup> While the DLA model does not provide a satisfactory description of the metal aggregates of Forrest and Witten,<sup>9</sup> it is one of the most studied aggregation models. In the basic Witten and Sandler<sup>8</sup> model, particles are added one at a time to a growing cluster, or aggregate, of particles. Particles are released at a very large distance from the cluster and follow random walk trajectories. If the particle contacts the cluster during its random walk then it becomes part of the growing cluster. If, however, the wandering particle leaves the lattice the trajectory is terminated to save computer time, and a new particle is launched. However, this model does not represent well most colloidal aggregation processes. In the early stages of colloidal aggregation the system consists of a large number of dispersed particles which move randomly in the fluid. As the particles continue to move through the fluid, they may come into contact with and stick to each other. The small clusters formed in this way continue to move and collide with other clusters and particles to form larger clusters. Therefore, this process is known as cluster–cluster aggregation.<sup>10</sup> As will be described below, it is believed that this type of growth algorithm is best able to describe the early stages of the growth of the silica film.

**Cluster–Cluster Aggregation (CCA).** Meakin<sup>10</sup> proposed a simple algorithm for the growth of CCAs. In this aggregation process, successively larger clusters are formed by the diffusion and aggregation of smaller particles. Initially, a fraction of the

sites of a square lattice of size  $L^2$  are occupied randomly while avoiding multiple occupancy. Occupied nearest-neighbor sites are considered to belong to the same cluster. Clusters, including single particle clusters, are then picked at random and moved one lattice step in one of the four equally probable directions in two-dimensional space. Even this simple algorithm can have a number of potential variants. The clusters can be randomly selected with probabilities that are (a) inversely proportional to cluster size, (b) independent of cluster size, or (c) directly proportional to cluster size. For reasons that will be given below, algorithm (c) was used in the work described here. In addition, biases can be added in favor of one or more of the various potential directions chosen for cluster movement. In a CCA, if a moving cluster contacts another cluster, the contacting clusters are immediately merged to form a larger cluster. This process of cluster–cluster aggregation is thus only a special case of the more generalized process known as reaction-limited (cluster) aggregation (RL(C)A).<sup>6</sup> In RLCA the cluster merging process is only allowed to occur with a probability  $p$ , where  $p$  takes some value between 0 and 1. In the work described here  $p$  has the upper limiting value of unity and the cluster growth is thus by the process of cluster–cluster aggregation. In this manner, the clusters grow in size until only one large cluster remains. Hence, it can be seen that there are a variety of potential aggregation algorithms, with different overall mechanisms, that may describe a given system, and each different type of algorithm also has a number of potential variants that may apply to a particular physical situation. To model a particular real system it is necessary to know which variant of which algorithm is appropriate in that case.

The CCA assimilation process has previously been suggested as a model for the gelation process in the sol–gel synthesis of glasses and ceramics, in which hydrolysis and polycondensation reactions polymerize the monomer into oligomers.<sup>6</sup> The repetition of such a process leads to the formation of the sol, and the gelation is performed either by aggregation or cross-linking. The overall size of the liquid surface, on which the silica film was grown in this work, is many orders of magnitude larger than the size of the initially precipitated silica particles that go on to aggregate into a film. Due to computing limitations it is not possible to carry out simulations on a model grid that represents the whole of the surface of the liquid. Therefore, to remove edge effects with the smaller model lattices on which the aggregation process is simulated, the model lattices are considered to have so-called periodic boundary conditions. In the simulations of aggregation, occurring on lattices with periodic boundary conditions, clusters of occupied lattice sites that are caused to leave the lattice at one edge (e.g. the north side) by a cluster move step will reappear, moving back onto the lattice, at the opposite edge (e.g. the south side). However, in simulations of aggregation according to particular algorithms, taking place on lattices of finite size, the character of the cluster growth will still be influenced by the lattice size even when edge effects are removed by periodic boundary conditions. In particular, where clusters are selected for each cluster move step in the algorithm according to scheme (c) above, the overall geometry of the final cluster may be influenced by lattice size. This occurs for several reasons. Under scheme (c) the probability that a particular occupied site (whether it belongs to a cluster or not) will be selected at a particular move step is equal to  $1/\rho L^2$ , where  $\rho$  is the fraction of the total number of lattice sites that are occupied. Therefore, in the early stages of cluster growth, where many occupied sites are single particle clusters, a single particle cluster will change position, with respect to

the fixed grid frame and the overall sea of particles, less often on a larger lattice than on a smaller lattice. In the later stages of cluster growth (when most particles belong to a single large cluster), at a particular value of the remaining number of single particle clusters, the individual single particles will move around, with respect to the lattice itself and the main large cluster, less often on a larger lattice than on a smaller lattice. Under scheme (c) if a single particle that belongs to a much larger cluster is selected, at random, for movement then the whole cluster to which it belongs is also moved at the same time. Hence, under scheme (c), the larger that the overall lattice size is, then the more likely it is that the main cluster will, itself, sweep up any remaining smaller particles (small clusters), rather than having these smaller particles individually attach themselves to the main cluster. Therefore, in simulations according to scheme (c) on a lattice with periodic boundary conditions, a variation of the lattice size parameter is equivalent to varying the relative mobility of different cluster sizes on an infinite lattice. However, the function  $1/L^2$  becomes relatively flatter at larger values of  $L$ , and thus the sensitivity to lattice size decreases with larger lattices.

**Fractal Dimensionality, Lacunarity, and Correlation Length.** For a statistically self-similar fractal a measure  $\mu(l)$  within a distance  $l$  from a point on a fractal object is given by:

$$\mu(l) = \Lambda \cdot \mu(\epsilon) \cdot (l/\epsilon)^D \quad (1)$$

where  $\mu(\epsilon)$  is the measure of an occupied region of size  $\epsilon$ ,  $\Lambda$  is a constant that will be discussed below, and  $D$  is the power-law exponent known as the fractal dimension. In the systems of interest in this work, the measure  $\mu$  corresponds to the total mass  $M$  and the length scale  $l$  corresponds to the overall size (length scale)  $L$ . In this case:

$$M = \Lambda_M \cdot m \cdot (L/\epsilon)^D \approx L^D \quad (2)$$

where  $\Lambda_M$  is an amplitude, or shape factor, related to the lacunarity (see below) and  $m$  is the mass of a particle of size  $\epsilon$ . This scaling relationship between mass and size is consistent with the corresponding scaling relationship,  $M \approx L^d$ , for Euclidean objects embedded within Euclidean spaces of dimensions of  $d = 1, 2, 3$ . From eq 2 it is therefore clear that the number of particles,  $N$ , of size  $\epsilon$  within a distance  $L$  of a point on an object is given by:

$$N = \frac{M}{m} = \Lambda_M \cdot (L/\epsilon)^D \approx L^D \quad (3)$$

One of the simplest methods used to determine the fractal dimension of a fractal is known as “box-counting”. In this methodology, the fractal lying in  $d$ -dimensional Euclidean space is covered by a  $d$ -dimensional grid with grid elements of size (length scale)  $l$ . The box-counting, or capacity, dimension is then given by:

$$D_B = -\lim_{l \rightarrow 0} \log(N(l/L)) / \log(l/L) = \lim_{l \rightarrow 0} \log(N(l/L)) / \log(L/l) \quad (4)$$

where  $N(l/L)$  is the number of nonempty grid elements. In practice it is not possible to approach the limit  $l \rightarrow 0$ , so  $D_B$  is estimated by measuring the dependence of  $\log(N(l/L))$  on  $\log(l/L)$ , for length scales in the range  $l_1 < l < l_2$ , where  $l_1 > \epsilon$  (the lower cutoff) and  $l_2 < L$  (the upper cutoff):

$$D'_B = -\langle d(\log(N(l/L))) / d(\log(l/L)) \rangle_{l_1 < l < l_2} \quad (5)$$

The lacunarity may be estimated from the intercept.

Fractals with large values of the amplitude  $\Lambda_M$  fill space more uniformly, and they are said to be less lacunar. The amplitude  $\Lambda_M$  can be used to characterize quantitatively the lacunarity. Both the lacunarity and fractal dimensionality are needed to describe how a fractal object fills space and therefore to fully characterize the geometry of the object. Therefore, in this work, to determine whether a particular simulated fractal is a good model for a real fractal it will be required that both the lacunarity and fractal dimension of the simulated object are identical with the corresponding parameters for the real object.

In addition, in many real objects there is generally an upper length scale cutoff ( $\xi$ ) that can be smaller than the overall size of the object, but above which the fractal scaling law no longer holds. This upper length scale cutoff represents a so-called correlation length above which the structure may be considered homogeneous and Euclidean. At levels of inspection above the correlation length the object consists of (statistical) copies of the structure found below the correlation length, and statistical parameters such as the density or voidage fraction of the object are constants. The fractal scaling law only applies for levels of inspection below the correlation length, and thus an analogous version of eq 3 is obtained:

$$N(l/\xi) = n \Lambda_M \cdot (\xi/l)^D \quad (6)$$

where  $\Lambda_M$  is the lacunarity and the parameter  $n$  takes into account the number of (statistical) copies of the fractal region that are contained within the overall size of the object,  $L$ . In eq 5,  $l$  may be measured in any units and thus an alternative form is:

$$D'_B = -\langle d(\log(N(l/\xi))) / d(\log(l/\xi)) \rangle_{l_1 < l < l_2} \quad (7)$$

For a real object using square boxes for box-counting on a square overall grid the total number of boxes of size  $(l/\xi)$  required to cover the grid is given by:

$$N_T = \left(\frac{L}{l}\right)^2 = n \left(\frac{\xi}{l}\right)^2 \quad (8)$$

Dividing eq 6 by eq 8 gives:

$$\left(\frac{N}{N_T}\right) = \Lambda_M \left(\frac{\xi}{l}\right)^{(D-2)} \quad (9)$$

Hence, for  $l < \xi$ ,

$$D = \frac{d(\log(N/N_T))}{d(\log(\xi/l))} + 2 \quad (10)$$

The correlation length may be measured by means of an autocorrelation function  $C(s)$ .  $C(s)$  measures the degree of correlation between  $f(x_n)$  values at successive data points. Explicitly, defining  $\delta f_n$  as:

$$\delta f_n = f(x_n) - \langle f \rangle \quad (11)$$

then:

$$C(s) = \frac{\langle \delta f_n \delta f_{n+s} \rangle}{\langle \delta f_n^2 \rangle} \quad (12)$$

where the averages denoted by the brackets  $\langle \rangle$  are over the data set  $\{x_n\}$  (equivalent to the set of sites in the model grids). In the context of the model grids,  $f(x_n)$  is the value of the occupancy in site  $x_n$ . The occupancy is defined to be equal to 1 if the site



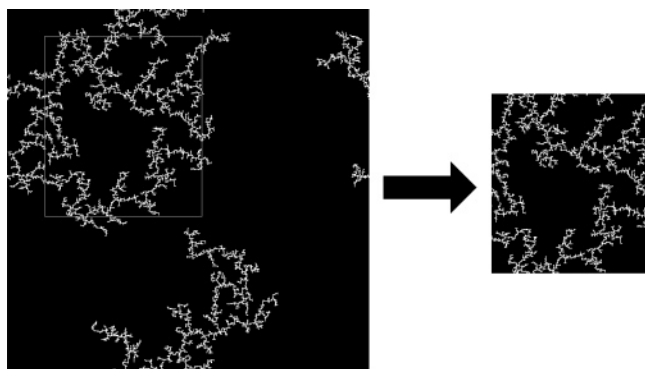


**Figure 1.** Schematic diagram of the creation of a simulated image from a model lattice.

is occupied, and equal to 0 otherwise. For eq 12 successive annular shells at a distance  $s$  from each site are considered for each site in turn. The characteristic values of this function are the value of  $C(s=1)$  and the value of  $s$  when  $C(s)=0$ . The first value characterizes the degree of correlation, while the second value is known as the correlation length ( $\xi$ ) and characterizes the linear extent of that correlation. If two fractal objects are identical then their correlation lengths must be identical.

In real systems the crossover from fractal to Euclidean behavior does not occur abruptly at the correlation length. For real fractal structures the transition is often more smeared out, and the fractal dimension appears to vary with length scale of inspection, and tends to the Euclidean limit as the correlation length approaches. The particular nature of its crossover behavior is another characteristic peculiar to a specific fractal object, and can also be used to assess the validity of a given model.

**Model Validation Method.** As described above, the raw experimental data consist of snapshots taken of only a section of the whole liquid surface in the trough. Therefore, this feature of the experiment will be simulated by growing model clusters on very large grids and then excising a section of the grid on which the statistical analyses will be performed, as shown schematically in Figure 1. Since the size of one site in a potential model grid and the pixel resolution of the raw experimental images do not necessarily correspond, then an alternative means by which to achieve spatial equivalence between them will be used. As mentioned above, if a simulated fractal is a good model for a real object then the correlation lengths of each should be in complete correspondence. The individual correlation lengths for each of the model and real images can each be obtained in terms of the respective lattice units of the grid they occupy. When each potential model grid is tested it initially assumed that the correlation lengths of the model and real image are exactly equivalent in absolute terms. Thus, a common yardstick for all length scales measured in either grid can then be established by using dimensionless, reduced lengths. The reduced lengths for length scales in a given grid are obtained by dividing a particular length, as measured in numbers of sites of that particular grid, by the correlation length for the same grid, as measured in units of the lattice sites for that grid. Hence, the correlation length can be used to calibrate the unit conversion between the length scale represented by a real image lattice site and that equal to a model grid site. Therefore any length scale in a model grid will be actually identical with that in the real image grid if they each have equal values when expressed in the appropriate reduced units for their grid. Hence, identical values for box side lengths taken from the box-counting results for each grid will actually be equal if each box side length is

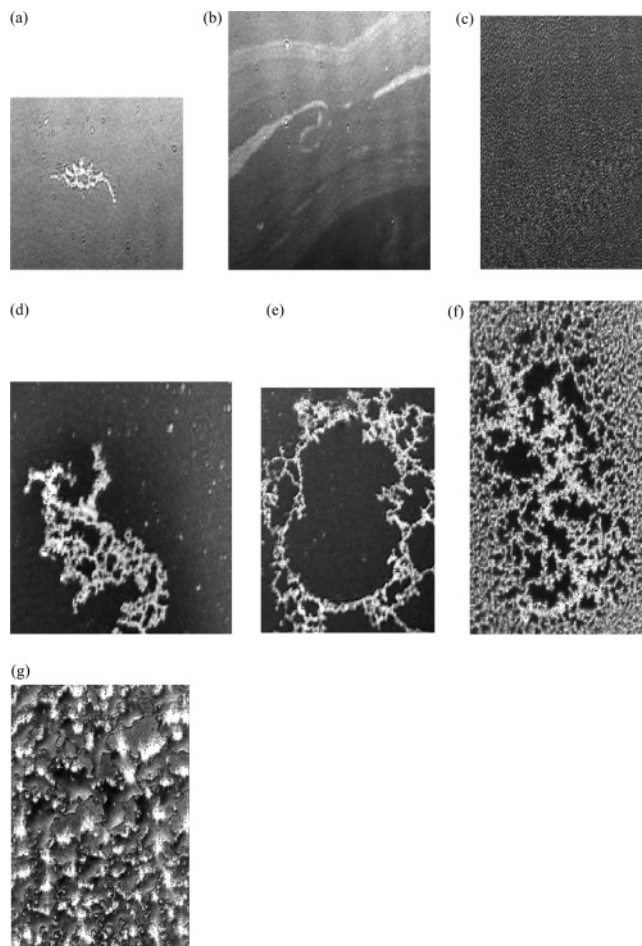


**Figure 2.** Brewster angle micrographs of the different stages of the silica film growth process described in the text.

expressed in the appropriate reduced units. Therefore, if the relevant length scales are expressed in reduced units *and* the simulated cluster grid is a good model for the real image, then both the box-counting data, and the overall form of the autocorrelation function should match. In particular, if  $\log(N/(l/\xi))$  against  $\log(l/\xi)$  plots of the respective box-counting data for the model and real image grids match, then the model and real images must be characterized by the same fractal dimension- $(s)$ , lacunarity, and fractal-Euclidean crossover behavior. Hence, a cluster aggregation simulation may be validated as a good model for the real system by making this comparison.

## Results

**General Experimental Observations.** The general visual observations made during the course of a typical experiment are described below. In the description given, the letters refer to the parts of Figure 2 that show an example of a typical image obtained at that particular stage of the experiment. In the images the silica particles are generally white or gray, while the liquid surface is black.

Initially, there is an induction period, of extended (246 min) duration, after the start of the experiment before the growth of the main silica film commenced.

(a) During this induction period, surface impurities can act as nucleation points for silica particles. These impurities consist of airborne particulates, usually fibers. These small fibers can be clearly seen floating on the surface of the solution and after a short period become decorated with bright spots suggesting that nucleation had occurred along the fiber. These nucleated

silica particles were observed after a relatively short period of time. This is in contrast to the formation of the silica film itself, which occurred much later in the experiment. It was noted that the nucleation points appeared to cause only a small amount of silica to precipitate out of solution and in all cases the silica was directly attached to the fiber. These early agglomerates did not initiate the formation of an extended silica film. Figure 2a is an image of an example of the silica particle that forms as a result of an impurity on the surface of the solution.

(b) During the induction period, “milky” swathes of silica were also observed to appear on the surface of the solution. The exact cause of these structures is not known. However, it is conjectured<sup>11</sup> that they may be caused by changes in tail orientation of the surfactant or phase separation at the solution surface. Figure 2b shows an image of examples of this phenomenon. In most cases these formations disappear before the main body of silica precipitated out of solution; however, in the case of fractal films they can sometimes be seen underlying the brighter fractal structures on the surface.

(c) Some time (after 246 min) into the experiment a large amount of silica was seen to precipitate over the relatively short period of 15 min. Numerous fine particles rose to the surface of the solution. The particles were observed to move around the surface in random Brownian motion. Particles were observed to collide with other particles to form larger particles. This stage in the experiment is illustrated in Figure 2c. It was these larger particles that began to form fractal clusters.

(d) Fractal patterns did not appear uniformly across the solution surface. Figure 2d shows an example of an early fractal cluster that is surrounded by a region of darkness in the image which corresponds to a zone that is relatively lacking of silica particles compared to the rest of the solution surface. However, the fractal cluster and the depleted region are, themselves, enveloped by a larger, outer region containing a mist of fine silica particles and small aggregates.

(e) As the experiment proceeded, more open fractal clusters, such as the one shown in the image in Figure 2e, appeared as the aggregates joined together into larger and larger groups.

(f) At the latter stages of the experiment, it was observed, even by eye, that particular areas within a single image had distinctly different fractal geometries. Figure 2f shows an example of a region containing a lacy, open fractal structure enveloped within a much denser fractal lattice.

(g) The density of the structures on the surface of the solution increased with time until a semicontinuous film was formed. An example of such a film is shown in Figure 2g.

The formation of the small silica aggregates from airborne contaminants and milky swathes occurring at the early stages of the experiment did not have any apparent influence on the later stages of film growth and so will be neglected in the simulations of film growth below. Milky swathes have been present during film growth for most films observed using Brewster Angle Microscopy in these and previous studies,<sup>11</sup> whatever the surfactant used, and at every concentration. The surface pressure has been measured and there is generally a slight increase in surface pressure about the same time as the swathes appear, suggesting that something is adsorbed to the interface. However, the surface pressure then decreases again while the swathes are still visible, though the solution surface becomes briefly homogeneous before solid film formation begins (whether as fractal or continuous films). There is no change in the off-specular X-ray scattering signal when the swathes become visible so there is no ordered phase at the interface. At certain concentrations, specular X-ray scattering

indicates the formation of layers at the interface prior to film formation. However, the swathes are visible even at concentrations where these layers do not occur. Possibly the swathes are due to areas of different surfactant tail orientation in the surfactant surface excess relative to the polarized laser beam which probes the surface. Brewster Angle Microscopy is sensitive both to surface film thickness and orientation, though there is no way to deconvolve these two contributions in the grayscale images. There is no excess nucleation of particles in regions where the milky swathes were visible (although, since the swathes are mobile, and also disappear just before film formation occurs, it is difficult to relate particle formation to swathes). Particle formation appears to be more or less uniform over the surface of the solution visible in the window viewed by the Brewster Angle Microscope ( $\sim 1$  mm diameter spot), although particle packing clearly becomes more dense in some regions and less dense in others after the initial burst of particle formation.

The overall scenario observed in the experimental studies, consisting of the (relatively) sudden formation of many individual silica particles which then undergo random motion and aggregation to form open, lacy fractal objects, seems to share the same main characteristic processes with the CCA growth algorithm described above. These general observations therefore suggest the possibility that the early stages of film growth occur by cluster-cluster aggregation. More specific features of the growth algorithm may also be determined from particular observations made during the experiments. As mentioned above, a boundary zone, consisting of a region of liquid surface that had been depleted of small silica particles (appearing in the micrograph images, such as Figure 2d, as darker patches of liquid surface), was generally observed surrounding (relatively) larger fractal aggregates. This observation has suggested that, during the initial film growth, larger fractal aggregates were “sweeping up” smaller silica particles, rather than growing by “bombardment” from the surrounding cloud of smaller particles. If the growth of larger clusters had, instead, been predominantly occurring by the “diffusion in” of smaller particles toward the larger cluster, then it would be expected that small particles would occupy the liquid surface right up to the edge of the larger cluster. However, if the larger clusters had been moving around relative to the surrounding cloud of smaller particles, then it is likely that smaller particles would have been “swept up” by the extended tendrils and branches of the larger cluster as they moved through the cloud of smaller particles. This sweeping process would also be expected to leave a temporary “wake” of empty liquid surface which would remain clear until the (relatively) slower random motions of the smaller particles caused the re-occupation of the empty surface. This particular finding suggests that variant (c) of the CCA algorithm described above is probably the most appropriate version for the system studied here because of the relatively higher mobility of larger compared to smaller clusters when using that particular algorithm. The lattice size then gives a quantitative parameter that is related to the relatively higher mobility of larger over smaller clusters.

**Image Analysis of Brewster Angle Micrographs.** The focal plane of the Brewster angle microscope has a finite thickness and the individual silica particles precipitated from solution are not true 2D particles since they also possess a finite thickness. The silica particles are roughly spherical, and can be of slightly different sizes and also positioned at slightly different levels with respect to the focal plane. The result of these facts is that the boundary between the white pixels corresponding to solid



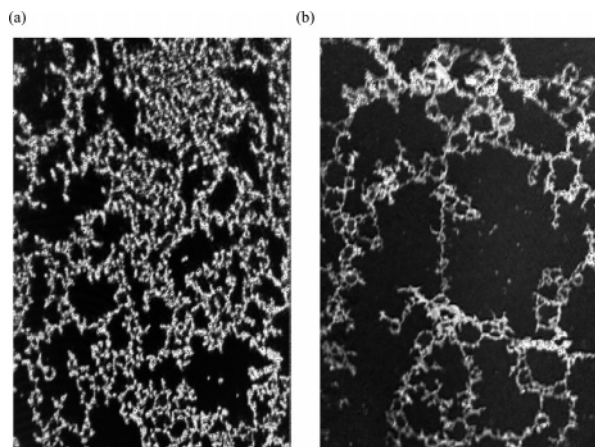


**Figure 3.** Brewster angle microscope images of two different silica clusters analyzed in this work. The horizontal side length of each image corresponds to  $430\ \mu\text{m}$ .

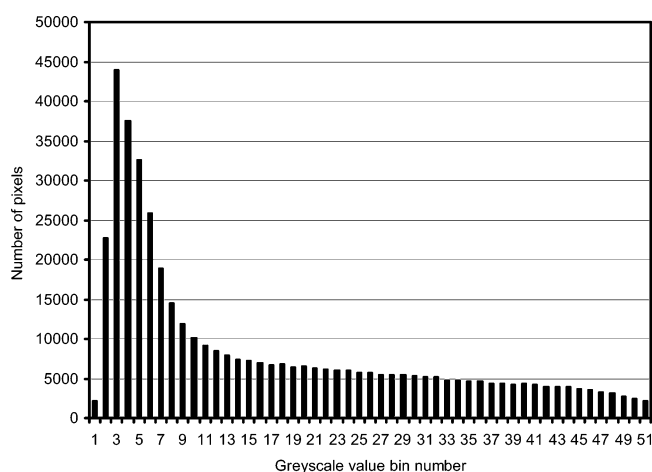


**Figure 4.** Histogram showing the numbers of pixels in Figure 3a falling into the various different bins for gray levels. Bins consist of 5 successive gray levels, e.g. bin 1 contains gray levels 0–4, bin 2 contains gray levels 5–9.

particles and the black pixels corresponding to empty liquid surface is made up of layers of pixels with various degrees of grayness. Hence, there is not an immediately obvious, clear demarcation between which pixels correspond to solid particles and which pixels correspond to empty liquid surface. To conduct the same fractal analysis on the real silica clusters as will be carried out on the simulated structures it is necessary to gate the micrograph images. In the gating procedure a particular gray level is selected and any pixels with intensities above this value are considered as white, and therefore solid, while any pixels with intensities below the threshold level are considered as black, and therefore as liquid surface. The particular choice of gating threshold level will affect the solid fraction ( $= 1 - \text{voidage fraction}$ ) of the image and the shape of the cluster, and, therefore, also affect the values of the characteristic parameters that will be obtained from the analysis of the gated image. To properly compare real and simulated clusters, it is necessary to obtain statistical parameters from the real images that are truly characteristic of the real cluster and, hence, independent of arbitrary parameters such as gating level. It is therefore necessary to obtain an algorithm for the objective selection of the threshold gray level.

In the experiments a series of many micrographs was obtained over time. To illustrate the general process carried out for all of the large number of cluster images obtained, two specific

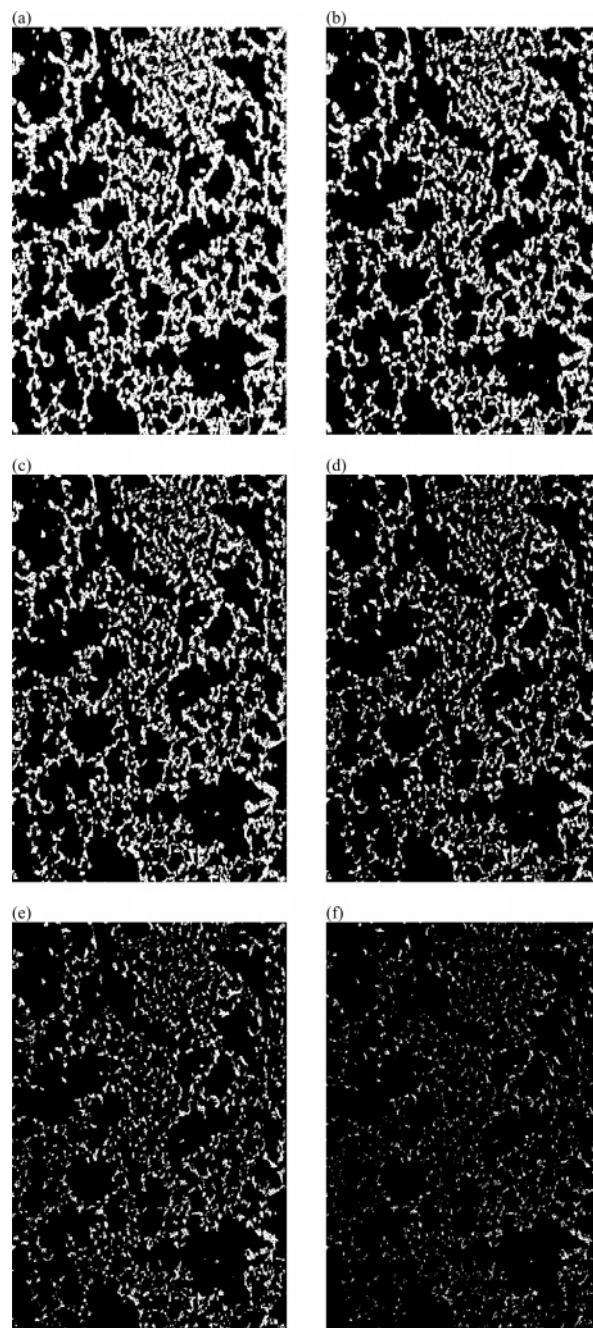


**Figure 5.** The results of gating the image in Figure 3a at various different gray levels. The cutoffs between black and white pixels were set at (a) 100, (b) 125, (c) 150, (d) 175, (e) 200, and (f) 230.

examples will be analyzed in the particular work described here. These images are shown in Figure 3. These images were obtained at slightly different times in the film growth experiments. Figure 4 shows a histogram of the grayscale values in Figure 3a. It can be seen that the histogram is not bimodal, as might be expected for a clear solely black and white image, and is therefore no aid to the selection of the most appropriate grayscale threshold level.

To determine the appropriate objective choice of grayscale threshold for the gating procedure the following methodology was used. Each of the raw micrograph images was gated at a series of grayscale values. An example of the series of lattices obtained by gating the raw image shown in Figure 3a at various different grayscale values is shown in Figure 5. Once the gated images were obtained, these images were analyzed by using

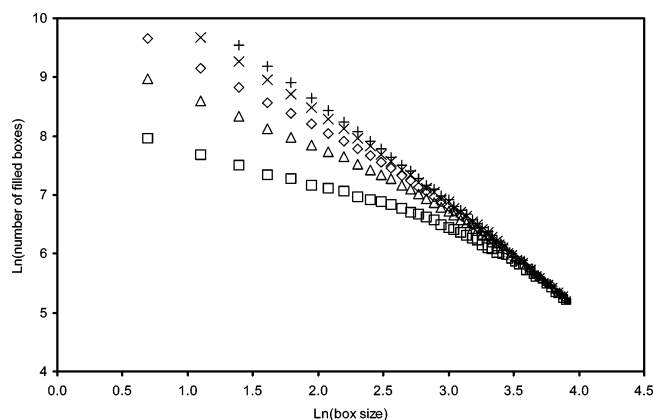


**Figure 6.** The relationship between the number of boxes containing the cluster and the box size for the gated images in Figure 5. The gating levels were 100 (+), 150 (x), 200 (◇), 230 (△), and 250 (□).

**TABLE 1: The Fit Parameters Arising from the Fitting of Eq 3 to the Box-Counting Data for Boxes in the Size Range 31–50 Pixels Square for the Images Shown in Figure 5, and Analogous Gated Images Derived from the Raw Image in Figure 3b<sup>a</sup>**

image	gating level	solid fraction <sup>b</sup>	fractal dimension	$\ln \Lambda_M$	coeff of determination, $r^2$
Figure 3a	100	0.327	$1.86 \pm 0.03$	12.52	0.99
	125	0.258	$1.84 \pm 0.04$	12.46	0.99
	150	0.196	$1.84 \pm 0.03$	12.43	0.99
	175	0.140	$1.81 \pm 0.03$	12.32	0.99
	200	0.090	$1.81 \pm 0.03$	12.31	0.99
	230	0.037	$1.75 \pm 0.03$	12.08	0.99
	250	0.011	$1.62 \pm 0.04$	11.52	0.99
Figure 3b	100	0.213	$1.57 \pm 0.03$	11.29	0.99
	125	0.159	$1.54 \pm 0.03$	11.14	0.99
	150	0.114	$1.57 \pm 0.04$	11.20	0.99
	175	0.078	$1.46 \pm 0.04$	10.74	0.99
	200	0.048	$1.29 \pm 0.03$	10.01	0.99
	230	0.021	$1.18 \pm 0.05$	9.38	0.99
	250	0.007	$0.88 \pm 0.06$	7.93	0.99

<sup>a</sup> The errors quoted are one standard error and were obtained from the linear regression of the raw box-counting data. <sup>b</sup> Number of white pixels/total number of pixels.

the box-counting algorithm described above. The box sizes used in the box-counting procedure were in the range from one pixel up to a size of the same order as the whole image. The fractal dimension applying over a particular range of length scales was estimated from the slope of the straight-line fit to the appropriate segment of the plot of  $\log(N(l))$  against  $\log(l)$ . The lacunarity was obtained from the intercept of the fitted straight line, using the logarithmic form of eq 3. Figure 6 shows an example of the set of relationships, between the number of boxes containing a cluster and the size of the box, obtained for processed images obtained by gating the raw image shown in Figure 3a at various different gray levels (see Figure 5). For each gated image, separate straight-line fits were made to the box-counting data for box sizes in the ranges of 2–30 and 31–50 pixels. Tables 1 and 2 show the fractal dimensions, lacunarities, and solid fractions (number of white pixels/total number of pixels) obtained from the box-counting analysis of the raw images shown in Figures 3a and 3b after each has been gated at various levels. It can be seen from Figure 6, and Tables 1 and 2, that the fractal dimensions and lacunarities obtained, for each gated image, from straight-line fits to the box-counting data over the range of box sizes between 31 and 50 pixels are generally independent of gating level, except for extremely high threshold values. It can also be seen from the data given in Tables 1 and

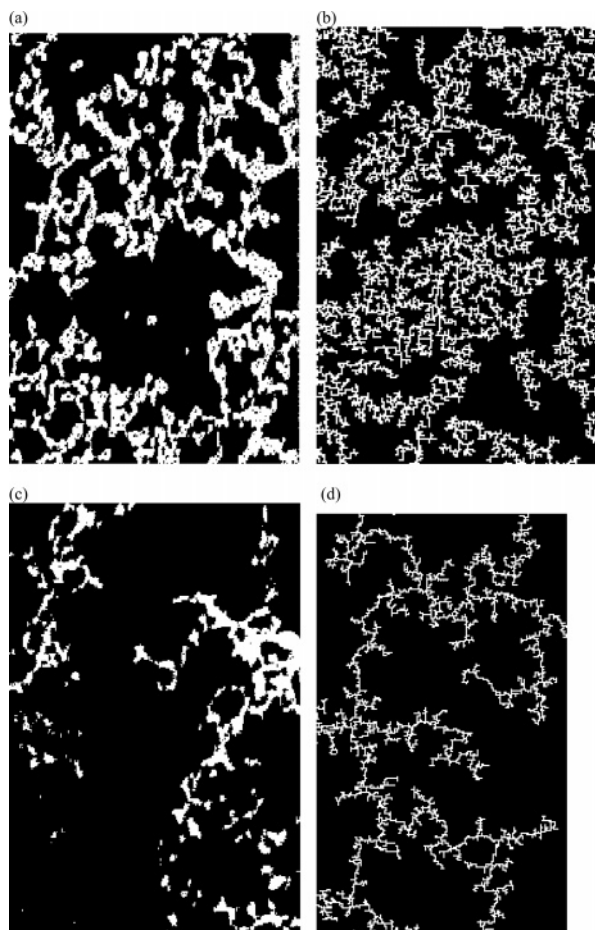
**TABLE 2: The Fit Parameters Arising from the Fitting of Eq 3 to the Box-Counting Data for Boxes in the Size Range 2–30 Pixels Square for the Images Shown in Figure 5, and Analogous Gated Images Derived from the Raw Image in Figure 3b<sup>a</sup>**

image	gating level	solid fraction <sup>b</sup>	fractal dimension	$\ln \Lambda_M$	coeff of determination, $r^2$
Figure 3a	100	0.327	$1.66 \pm 0.01$	11.87	0.99
	125	0.258	$1.60 \pm 0.01$	11.67	0.99
	150	0.196	$1.52 \pm 0.01$	11.42	0.99
	175	0.140	$1.44 \pm 0.02$	11.12	0.99
	200	0.090	$1.31 \pm 0.02$	10.71	0.99
	230	0.037	$1.07 \pm 0.02$	9.89	0.99
	250	0.011	$0.71 \pm 0.02$	8.55	0.99
Figure 3b	100	0.213	$1.57 \pm 0.01$	11.31	0.99
	125	0.159	$1.53 \pm 0.01$	11.08	0.99
	150	0.114	$1.48 \pm 0.01$	10.83	0.99
	175	0.078	$1.39 \pm 0.01$	10.50	0.99
	200	0.048	$1.28 \pm 0.01$	10.04	0.99
	230	0.021	$1.09 \pm 0.01$	9.22	0.99
	250	0.007	$0.88 \pm 0.01$	8.12	0.99

<sup>a</sup> The errors quoted are one standard error and were obtained from the linear regression of the raw box-counting data. <sup>b</sup> Number of white pixels/total number of pixels.

2, but also visually in Figure 6, that, as the gating level for a particular raw image is decreased, the fractal dimensionality and lacunarity, obtained from the box-counting analysis of the gated image with box sizes in the range 2–30 pixels, tend asymptotically toward limiting values, and closer to the corresponding values of the fractal dimension and lacunarity parameters generally obtained for most gating levels over box sizes of 31–50 pixels. It is therefore suggested that the most appropriate and objective threshold gating level for each raw image is the grayscale value, which leads to the limiting values and the closest similarity between the values of both the fractal dimension and the lacunarity obtained from separate straight-line fits to the results of box-counting analysis with box sizes in the ranges of 2–30 and 31–50 pixels. It can be seen that for all examples of raw micrograph images shown here the appropriate threshold level for the gating procedure selected by this method is 100–125. It is noted that the asymptotic values of the fractal dimension for Figure 3a are a function of length scale (i.e. box side length) while those of Figure 3b are not. Figure 3a has a smaller correlation length than Figure 3b. Hence, since the fractal dimension of Figure 3a appears to increase, with increased length scale of inspection, toward the Euclidean value of 2, then it is likely that the box-counting data for Figure 3a are exhibiting signs of crossover effects, while those for Figure 3b are not.

Experimental images obtained around stage (e) of the overall film growth process were studied here since this period represents the final stages of cluster–cluster growth. Once the real images had been gated to a suitable value (as decided above) the autocorrelation function and box-counting data could be obtained as described in the Theory section. Periods (c) to (e) of the real film growth process were simulated by using the CCA growth algorithm, as described above, and potential simulated images of stage (e) were obtained from the final fractal cluster arising from the modeling. Since the initial experimental solid volume fraction of precipitated silica was unknown, solid volume fractions in the range 0.085–0.41 were used in the simulations. These values were chosen because, since the film growth process leads to local increases in silica particle concentration (as clusters form), it is thus known that the typical solid fraction in images of clusters at later stages of growth (e.g. stage (e)) represents an upper limit on the initial, overall



**Figure 7.** The examples of images compared in this work. Image (a), the bottom right quadrant of Figure 3a, was compared with image (b), while image (c), the bottom left quadrant of Figure 3b, was compared with image (d).

particle concentration. Hence, initial particle concentrations for simulations were chosen in the range of, and below, that typically seen for images of clusters at stage (e). The simulations were performed on lattices of a size of 512 by 512 sites. Particular regions of the cluster(s) resulting from the simulations were then cut out of the main grid, as described in the Theory section above, to simulate the real experimental data acquisition process, and thus provide simulated images. The correlation lengths and box counting data were also obtained for the simulated images. In the case of each image, real or simulated, the relevant correlation length was given a value of dimensionless length equal to unity. After making all length scales dimensionless, the autocorrelation functions and box-counting data for pairs of real and simulated images were compared.

Numerous statistical comparisons were made between real and simulated images, and many good matches were obtained. Two sets of typical examples of characteristic sets of real and simulated images that were compared statistically are shown in Figure 7. The real images show large fractal clusters and a small number of apparently isolated silica “particles” surrounded by the larger cluster. As may be seen by comparing Figures 3 and 7, for example, the real images generally show gray (rather than white) connections between the few isolated particles (seen in gated images) and the larger cluster. It is thus suggested that apparent disconnection of some particles in the gated image may arise because narrow “isthmus” links to the larger, neighboring cluster may be out of the focal plane (and thus become gated out). However, as described above the statistical

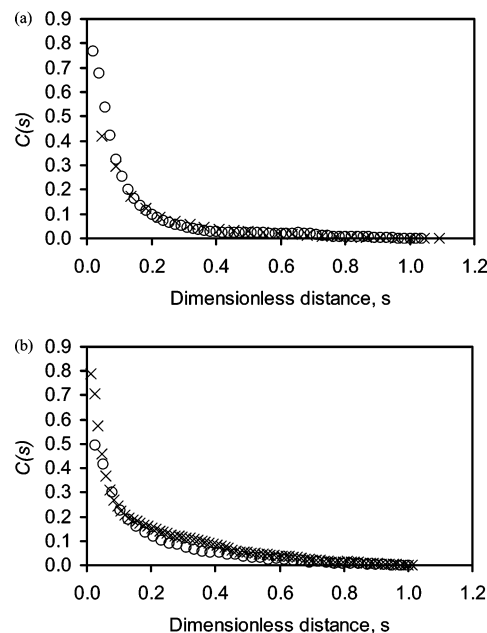


**Figure 8.** A comparison of the autocorrelation functions for the real ( $\times$ ) and simulated ( $\circ$ ) images in (a) parts a and b of Figure 7 and (b) parts c and d of Figure 7.

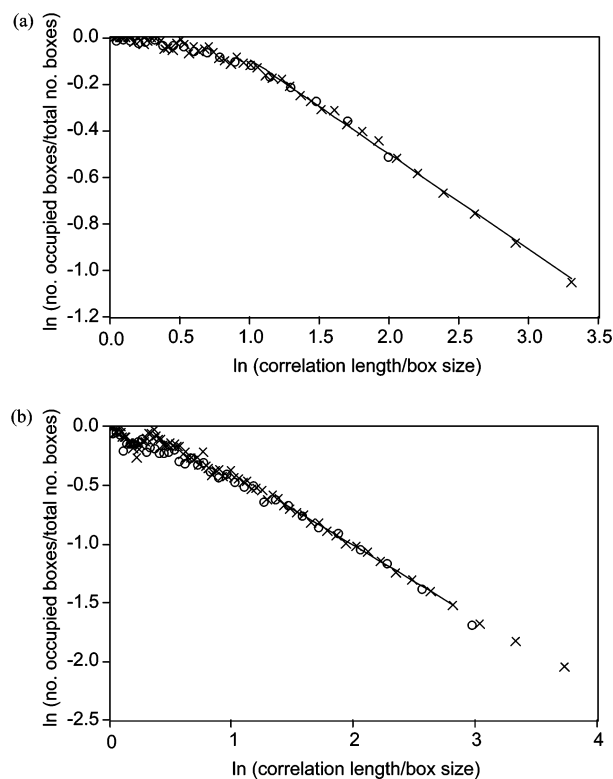


**Figure 9.** A comparison of the box-counting data for the real ( $\times$ ) and simulated ( $\circ$ ) images in (a) parts a and b of Figure 7 and (b) parts c and d of Figure 7. The solid lines shown are the fits of eq 9 to the data for real images given in Table 3.

parameters obtained from the gated real images are in the range insensitive to gating level.

The plots of the image autocorrelation functions against dimensionless length for the example sets of images are shown in Figure 8. It can be seen that, in each case, the forms of the variation of autocorrelation function with dimensionless length for the real and simulated images match very closely. Figure 9 shows comparisons of the box-counting data for each set of real and simulated images. In each case, the data for both the



**TABLE 3: The Fit Parameters Resulting from the Fit of Eq 9 to the Box-Counting Data for the Images Shown in Figure 7<sup>a</sup>**

image	fitted range in Figure 9	fractal dimension	$\ln \Lambda_M$	coeff of determination, $r^2$
Figure 7a	1–3.3	$1.59 \pm 0.01$	$0.316 \pm 0.015$	0.997
Figure 7b	1–2	$1.61 \pm 0.02$	$0.289 \pm 0.019$	0.986
Figure 7c	1.4–3	$1.38 \pm 0.01$	$0.230 \pm 0.013$	0.998
Figure 7d	1.4–3	$1.35 \pm 0.02$	$0.290 \pm 0.023$	0.996

<sup>a</sup> The errors quoted are one standard error and were obtained from the linear regression of the raw box-counting data.

real and simulated images show a linear region in the logarithmic plot in agreement with eq 9 that generally extends over a range of an order of magnitude in box side length where the data are available. Hence, both real and simulated images possess intervals in length scales where there is a fractal scaling regime. However, since there is a difference in the ratio of pixel resolution to correlation length between real and simulated images, then the intervals of fractal scaling differ in extent. The fractal dimensions and lacunarities obtained from fits of eq 9 to the data for real and simulated images are shown in Table 3. It can be seen that, within experimental error, the values of the fitting parameters (fractal dimension and lacunarity) are identical for real and simulated images.

From Figure 9, it can be seen that, as the dimensionless box size approaches a value of unity, there is a deviation from eq 9. This deviation from simple single fractal scaling behavior arises because of the commencement of the crossover in the structure between fractal and Euclidean geometry that occurs at the correlation length. For both real and simulated structures the crossover does not occur abruptly at the correlation length but there are more gradual increases in the scaling exponent (fractal dimension) and decreases in lacunarity with length scale toward the Euclidean values of 2 and 1, respectively. Comparing Figures 9a and 9b it can be seen that the particular form of the crossover behavior differs between the two sets of real and simulated images. However, from Figures 9a and 9b, by eye, it can be seen that the crossover behavior of the relevant simulated images matches well with that of the corresponding real images.

## Discussion

A given fractal structure is characterized by its particular values of fractal dimension and lacunarity, and also the form of its autocorrelation function and Euclidean crossover behavior. This collection of characteristic descriptors closely specifies a particular type of structure. It has been seen that the structures produced by the particular variant of the cluster–cluster aggregation algorithm described above possess the same statistical properties as the structures observed in experimental images of silica film growth. Hence, it is suggested that the CCA algorithm is a good model for stages (c) to (e) of the growth of the silica film.

The crossover between fractal scaling and Euclidean behavior, observed in both real and simulated silica structures at larger box side lengths, may represent the onset, at larger cluster length scales (and thus later growth times), of the coalescence of fractal clusters that eventually results in the more Euclidean geometry of the structure of the film observed during later stages of the film growth (stages (f) and (g)). Silica films may be “harvested” from the liquid surface at any stage in the synthesis, and fractal films thus obtained.

The CCA algorithm contains a number of internal parameters that may be changed in the simulations, such as the sticking

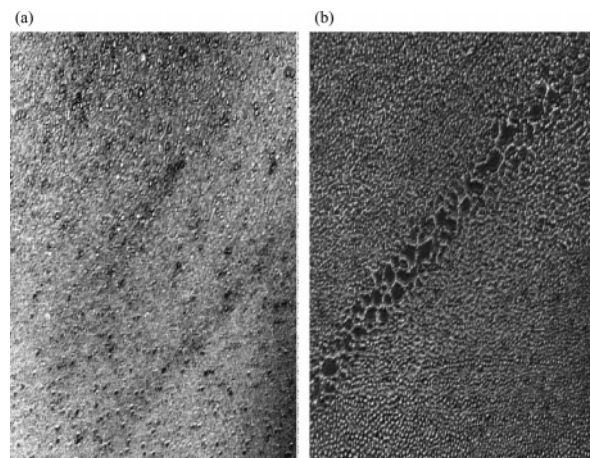


**Figure 10.** Images taken during the course of a silica film growth experiment with an altered silica concentration (TMOS/CpCl = 13.5). The images shown were obtained (a) shortly after the initial precipitation of silica particles and (b) during the next stage of film growth. The horizontal side length of each image corresponds to 430  $\mu\text{m}$ .

probability for particles on collision. These parameters have analogues in the real system that also could potentially be changed. Once one has determined that the mechanism of growth of the real silica film is CCA then it is possible to use the simulation to predict changes in the silica film growth if various parameters are changed. Preliminary work has been conducted on the effects of changing the sticking probability of particles. As mentioned above, if the sticking probability in a cluster–cluster aggregation is reduced below unity, the process becomes known as reaction-limited aggregation (RLA). In RLA the migrating particles and clusters no longer immediately bond with each other upon first contact, which generally occurs toward the outer extremities of clusters. Hence, single particles are thus able to penetrate more deeply into an existing cluster before becoming attached, and two colliding clusters can potentially interpenetrate each other more before becoming permanently bound together. These consolidation effects tend to lead to more compact clusters<sup>12</sup> that have properties that are more similar to Euclidean structures even from the start of growth. It is also possible to change the sticking probability in the experimental system. Silica film growth experiments can also be performed with approximately the same surfactant concentration as above but with a change in the silica concentration (TMOS/CpCl = 13.5). It is considered that this change leads to a decrease in sticking probability because there is then more surfactant present per silica particle, which then partially inhibits the tendency for the silica particles to stick together. It is proposed that two silica particles stick together during a collision because this event causes hydroxyl groups located on the surfaces of each particle to come into close contact. In these circumstances, the hydroxyl groups can then undergo an acid-catalyzed condensation reaction, similar to that occurring during gelation, thereby bonding the two particles together. However, any excess surfactant not contributing to the pore-templating will tend to adsorb as a coating on the outside of the silica particles (probably as a double layer) and thus obscure hydroxyl groups on the surface, and hence lower the sticking probability. Figure 10 shows images of the film growth obtained during an experiment performed with an altered silica concentration. Figure 10a shows the silica particles shortly after their initial precipitation. Figure 10b shows a typical image from the next stage in the film growth process. In this case, the film did not go through any intermediate stage with relatively more open fractal clusters but, instead, rapidly formed the much more dense

structures shown in Figure 10b. These experimental observations are in line with the expectations raised by past computer simulations of RLA.<sup>12</sup> Alternatively, the computer simulations could also be used to understand the effects of changes in the synthesis method. If a change is made to the synthesis which changes the macrostructure of the film generated, then the cause of that change in structure could, potentially, be deduced from the changes required in the simulation algorithm in order to mimic that structural change in the simulated model clusters. More detailed studies of the use of the computer simulation in the design of film syntheses in order to obtain films with particular, desired properties will be described in a subsequent publication.

## Conclusions

It has been shown that the silica cluster structures observed in Brewster angle micrographs of a silica film growth process possess many identical statistical properties to artificial fractal clusters grown on a computer using a particular variant of the cluster-cluster aggregation algorithm. Hence, it is proposed that the real silica film grows by the particular CCA mechanism used in the computer simulations. This may lead to the possibility of designing the film synthesis process using computer simulation.

**Acknowledgment.** The authors wish to thank Dr. Stephen Roser for the use of the Brewster Angle Microscope. K.J.E.

wishes to thank the Royal Society for the award of a Dorothy Hodgkin Research Fellowship.

## References and Notes

- (1) Aksay, I. A.; Trau, M.; Manne, S.; Honma, I.; Yao, N.; Zhou, L.; Fenter, P.; Eisenberger, P. M.; Gruner, S. M. *Science* **1996**, *273*, 892–898.
- (2) Yang, H.; Coombs, N.; Sokolov, I.; Ozin, G. A. *Nature* **1996**, *381*, 589–592.
- (3) Brown, A. S.; Holt, S. A.; Dam, T.; Trau, M.; White, J. W. *Langmuir* **1997**, *13*, 6363–6365.
- (4) Brown, A. S.; Holt, S. A.; Reynolds, P. A.; Penfold, J.; White, J. W. *Langmuir* **1998**, *14*, 5532–5538.
- (5) Brennan, T.; Hughes, A. V.; Roser, S. J.; Mann, S.; Edler, K. J. *Langmuir* **2002**, *18*, 9838–9844.
- (6) Brennan, T.; Roser, S. J.; Mann, S.; Edler, K. J. *Chem. Mater.* **2002**, *14*, 4292–4299.
- (7) Ruggles, J. L.; Holt, S. A.; Reynolds, P. A.; White, J. W. *Langmuir* **2000**, *16*, 4613–4619.
- (8) Ruggles, J. L.; Gilbert, E. P.; Holt, S. A.; Reynolds, P. A.; White, J. W. *Langmuir* **2003**, *19*, 793–800.
- (9) Ruggles, J. L.; Holt, S. A.; Reynolds, P. A.; Brown, A. S.; Creagh, D. C.; White, J. W. *Phys. Chem. Chem. Phys.* **1999**, *1*, 323–328.
- (10) Henderson, M. J.; King, D.; White, J. W. *Aust. J. Chem.* **2003**, *56*, 933–939.
- (11) Henderson, M. J.; King, D.; White, J. W. *Langmuir* **2004**, *20*, 2305–2308.
- (12) Schwartz, D. K.; Steinberg, S.; Israelachvili, J.; Zasadzinski, J. A. *N. Phys. Rev. Lett.* **1992**, *69*, 3354–3357.
- (13) Carrière, T.; Ortiz, C.; Fuchs, G. *J. Appl. Phys.* **1991**, *70*, 5063–5067.
- (14) Avnir, D., Ed. *The Fractal Approach to Heterogeneous Chemistry*; Wiley: Chichester, UK, 1989.
- (15) Edler, K. J.; et al. In preparation.
- (16) Witten, T. A.; Sandler, L. M. *Phys. Rev. Lett.* **1981**, *47*, 1400.
- (17) Forrest, S. R.; Witten, T. A. *J. Phys. A* **1979**, *12*, L109.
- (18) Meakin, P. *Phys. Rev. Lett.* **1983**, *51*, 1119–1122.
- (19) Edler, K. J.; Brennan, T.; Roser, S. J.; Mann, S.; Richardson, R. M. *Microporous Mesoporous Mater.* **2003**, *62*, 165–175.
- (20) Elias-Kohav, T.; Sheintuch, M.; Avnir, D. *Chem. Eng. Sci.* **1991**, *46*, 2787–2798.